Check for updates

Molten salt synthesis of carbon-supported Pt–rare earth metal nanoalloy catalysts for oxygen reduction reaction†

Yulin Jiang,[a] Tao Fu,*[b] Jiaxiang Liu,[c] Jinbao Zhao, [ID] *[ac] Bing Li[bd] and Zhenjie Chen[a]

The synthesis of nano-sized alloys of Pt and rare earth (RE) metal catalysts has been a huge challenge due to a significantly large standard reduction potential difference of Pt and RE metals and the high synthesis temperature. Pt_xY/C catalysts with an average particle size of around 21 nm, were synthesized by mixing K_2PtCl_4 with Y_2O_3 (a molar ratio of Pt : Y = 1 : 1) with a carbon support in a molten $LiCl-CaH_2$ system by a one-step molten salt synthesis method at 600 °C. The synthesis processes of the Pt_xY/C alloys are proposed as follows: Pt nanoparticles were first obtained by the reaction of K_2PtCl_4 and CaH_2 at 210 °C, then Y ions were preferentially reduced on the Pt nanoparticle surface by the reduction of CaH_2, followed by Pt_xY alloy formation in the molten $LiCl-CaH_2$ system at 600 °C. Molten LiCl provides a strong reducing environment and lowers the formation temperature of alloys. Pt_2Gd/C and Pt_2La/C were also obtained with Gd_2O_3 and La_2O_3 as the starting raw materials, respectively by using the same process. When investigated as an electrocatalyst for the oxygen reduction reaction (ORR), the half-wave potentials of Pt_xRE/Cs are all more positive than that of commercial Pt/C catalyst (*e.g.*, 0.905 V for $Pt_xY/$ C while 0.880 V for JM Pt/C), and the nano-sized Pt_xY/C alloy shows higher electrocatalytic activity toward the ORR and preferable catalytic durability with respect to JM Pt/C catalysts. This facile synthesis method provides an effective strategy for the preparation of Pt–RE based multicomponent nanoalloys, especially in large-scale production.

1 Introduction

Nowadays proton exchange membrane fuel cells (PEMFCs), directly generating electrical energy through hydrogen oxidation at the anode and oxygen reduction reaction (ORR) at the cathode,[1–3] have received extensive attention in renewable energy fields (*e.g.* fuel cell electric vehicles), due to their advantages of low pollution and high specific energy.[4–9] Nevertheless, the high cost of PEMFCs still restricts their widespread commercialization in which platinum (Pt) catalysts used at both anode and cathode electrodes account for about 40% of the

[a]State Key Laboratory of Physical Chemistry of Solid Surfaces, Collaborative Innovation Centre of Chemistry for Energy Materials, State-Province Joint Engineering Laboratory of Power Source Technology for New Energy Vehicle, Engineering Research Center of Electrochemical Technology, Ministry of Education, College of Chemistry and Chemical Engineering, Xiamen University, Xiamen 361005, People's Republic of China. E-mail: jbzhao@xmu.edu.cn

[b]College of Chemistry and Material Science, Fujian Provincial Key Laboratory of Clean Energy Materials, Longyan University, Longyan 364012, People's Republic of China. E-mail: tfu@lyun.edu.cn

[c]College of Energy, Xiamen University, Xiamen 361005, People's Republic of China

[d]School of Mechanical and Power Engineering, East China University of Science and Technology, Shanghai 200237, People's Republic of China

† Electronic supplementary information (ESI) available. See DOI: 10.1039/d1ra09400a

cost.[10] In particular, the cathode requires about 9–10 times as much platinum as the anode because of its sluggish oxygen reduction reaction (ORR). Nowadays, many researchers have proposed many strategies to solve this problem, including morphology control, nanoparticles and Pt-based alloys.[11–17]

Pt-based alloys that can adjust the electronic structure of Pt atoms, is one of the effective strategies to enhance the activity and stability with the reduced amount of Pt in many catalysis fields.[18–20]

In the past two decades, the Pt-late transition metals (LTMs, such as Fe, Ni, Co *etc.*) alloys have been widely studied[21] and have remarkably improved the catalytic activities.[22] However, the late transition metals are more likely to dissolve and dealloy in the acidic medium of PEMFCs over time[23] due to the lower alloy formation energy between Pt and LTMs,[24] which results in the decrease of activity and durability of the alloys. Therefore, selection of the Pt alloys with higher alloy formation energy is beneficial to resist dealloying and maintain high stability.[25,26]

More recently, Greeley and his coworkers predicted and demonstrated that the Pt-rare earth metal (RE) alloys showed a significant enhanced activity by using density functional theory (DFT) calculations and experiments.[27] Subsequently, Sung Jong Yoo[25,28] explained that the strong electronic synergetic interaction between Pt and RE atoms results in the d-band center of Pt downshift, which can reduce the adsorption

strength of oxygenated species (*O, *OH, *OOH) and ultimately improve the activity. In addition, compressive strains in the particle surface will be generated in the alloy because the atomic radius of rare earth metals are larger than that of Pt, which can lower the adsorption of reaction intermediates at the Pt sites, and adjust the binding energy of oxygenated intermediates and boost ORR activity.[25] The application of Pt–RE alloy catalysts can not only improve the catalytic activity of ORR, but also can reduce the loading of Pt.[29]

However, the chemical synthesis of Pt–RE alloys is very challenging because of the vast difference of standard reduction potentials between Pt and RE metals (e.g. +1.19 V for Pt^{2+}/Pt, −2.37 V for Y^{3+}/Y) and the high oxygen affinity of RE metal atoms.[30] Moreover, synthesis of Pt–RE alloys usually needs high temperatures. For example, Pt_5Ce alloy phase forms at 1529 °C according to the phase diagram.[31] Hence such high temperature makes it more difficulty to synthesize nano-sized Pt–RE alloys. In the past decade, many efforts have been devoted to synthesize Pt–RE alloy catalysts by a variety of methods, however, only a few researches have been proved to obtain Pt–RE alloys in a strict reduction environment.[29,30,32] Schwämmlein et al. prepared Pt_xY/C alloy via thermally reducing YCl_3 with commercial Pt/C catalyst under the atmosphere of highly purified H_2 at 1200 °C.[33] Kanady et al. synthesized Pt_3Y nanoalloy particles by heating the mixture of alkali metal triethylborohydrides (MEt_3BH, M = K, Na), $PtCl_4$ and YCl_3 to 200 °C in which MEt_3BH was used as the reducing agent.[34] Itahara et al. prepared Pt_5Ce nanoparticles by using sodium vapor as the reducing agent at 600 °C.[32] Recently, Kobayashi et al.[35] reported the Pt_2Y nanopowders with a reckoned particle size of 147.8 nm by molten salt synthesis (MSS), via mixing Pt with Y_2O_3 in a molten $LiCl$–CaH_2 system under Ar atmosphere at 600 °C, in which CaH_2 was used as the reducing agent.

Molten salts usually composed of inorganic salts, are non-toxic and harmless to the environment,[36] which can well disperse the reactants and products, especially can lower the alloy formation temperature.[37,38] Therefore, MSS can be regarded as a potential candidate for preparation of Pt–RE alloys.

Before MSS of Pt_2Y nanopowders, Kobayashi et al.[35] first prepared the precursor of Pt and Y_2O_3 mixture by using H_2PtCl_6 and Y_2O_3 as raw materials at 500 °C, which not only made the synthesis complicated, but also increased the particle size to more than 100 nm. So, here, we simplified the synthesis procedure in one-step by directly mixing the raw materials including K_2PtCl_4, Y_2O_3, Vulcan XC-72R, $LiCl$ and CaH_2, and then directly prepared Pt_2Y by heating the mixture to 600 °C. The Vulcan XC-72R is used as the carbon support of Pt_2Y alloy, which can significantly isolate the alloy particles and reduce the particle size to 21 nm. At the same time, we explored the synthesis mechanism of Pt_2Y nanoalloys in $LiCl$–CaH_2 molten salts and successfully prepared Pt_2La and Pt_2Gd alloys by using the same method. The obtained carbon-supported Pt–RE nanoalloys were used as the ORR catalysts, which showed more positive half-wave potentials than that of commercial Pt/C catalyst, e.g., 0.905 V for Pt_xY/C while 0.880 V for JM Pt/C.

2 Experimental

2.1 Main materials

The materials including lithium chloride ($LiCl$, ≥99%, AR, anhydrous), calcium hydride (CaH_2, 95%, AR) and RE metal oxides (Y_2O_3, Gd_2O_3, La_2O_3) were all obtained from Aladdin Company. Potassium tetrachloroplatinate (K_2PtCl_4, Pt (wt%) ≥ 46%) was supplied by Tianjin Meisco Chemical, 5 wt% Nafion ionomer solution by Dupont and the carbon support Vulcan XC-72R by Cobalt. The commercial Pt/C catalysts were supplied by Johnson Matthey (20 wt% for Pt content, simplified as JM Pt/C). All the materials were used as received without for further treatment.

2.2 Synthesis of carbon-supported Pt–RE nanoalloy particles (Pt_xRE/C)

Pt_xY/C was synthesized in molten $LiCl$–CaH_2 system by one-step MSS method. First, a precursor was obtained by mixing K_2PtCl_4 with Y_2O_3 in a molar ratio of Pt : Y = 1 : 1, in which the Y-rich ratio was used to ensure that all of the Pt salt were completely alloyed with RE. Next, a mixture was prepared by grounding the precursor with carbon support (Vulcan XC-72R), $LiCl$ and CaH_2 in a mortar with a weight ratio of precursor (including Vulcan XC-72R): $LiCl$: CaH_2 = 1 : 40 : 10. Then the mixture was placed in a furnace to remove air for 1 hour at room temperature by purge with Ar, and heated to 600 °C at a heating rate of 5 °C min^{-1}. Through holding 2 hours at 600 °C, the products was taken out by cooling off naturally to room temperature. The products including byproducts and excess reactants, such as Y_2O_3, CaH_2, $LiCl$ and CaO, etc. were leached by 1.0 M HNO_3 solution, washed with Milli-Q water and separated by centrifugation (10 000 rpm for 5 minutes) for three times in sequence. Finally, Pt_xRE/C samples were obtained by freeze drying that contained around 23% Pt content according to ICP analysis.

Pt_2Gd/C and Pt_2La/C are also prepared with Gd_2O_3 and La_2O_3 as raw materials, respectively by using the same process as above.

2.3 Physical characterizations

The crystal information of the samples was depicted by X-ray diffraction (XRD) method using the Mini Flex 600 X-ray diffractometer (Rigaku) with the radiation source of Cu Kα (λ = 0.15418 nm) with a scan rate of 5.0° min^{-1}. The crystal structure and the morphology of the samples were acquired by transmission electron microscope (TEM) method using the F-30 HRTEM (Holland FEI Tecnai) at 300 kV. The elemental mappings were also performed by the F-30 HRTEM (Holland FEI Tecnai) equipped with the energy dispersive X-ray spectroscopy (EDX). The X-ray photoelectron spectroscopy (XPS) was applied to analyze the valence state of the elements in samples on X-ray photoelectron spectrometer (Thermo Fisherto, United State) with an Al Kα X-ray monochromator. The C 1s spectrum (284.6 eV) was used to calibrate the binding energy (BE). Inductively coupled plasma (ICP, NCS Testing Technology, Plasma1000) was carried out to examine the elemental content (Pt). In order to determine the synthesis mechanism, the

reactants were analyzed using simultaneous thermal analysis (STA 449 F3 Jupiter) under an argon atmosphere with a heating rate of 5 °C min^{-1}.

2.4 Electrochemical measurements

Catalyst inks were prepared according to the follow steps. First, 2 mg of the catalysts or JM Pt/C were added to the solution composing of 990 μL ethanol and 10 μL of the 5 wt% Nafion ionomer solution to form a mixture. Subsequently, the mixture was dispersed by ultrasonic treatment for 3 hours to yield uniform catalyst suspension. Thereafter, aiming to form the catalyst thin film, the catalyst ink (10 μL) was cast to the polished rotating disk electrode (RDE, S = 0.196 cm^{-2}, PINE Instrument) and dried naturally. The loading amounts of Pt on the electrode surface were around 20.41–23.47 μg cm$_{Pt}^{-2}$.

The electrochemical performance tests were carried out on the CHI730E bipotentiostat (Chenhua Instrument Corporation, Shanghai) at room temperature. The traditional three-electrode system was conducted to measure the ORR electrochemical performance, in which the catalyst ink coated in RDE, KCl-saturated Ag/AgCl electrode and a graphite electrode, were used as the working electrode (WE), reference electrode (RE) and counter electrode (CE), respectively. The electrolyte was 0.1 M HClO$_4$ solution. All the potentials were normalized to the reversible hydrogen electrode (RHE) after the electrochemical tests according to the following equation:

$$E_{vs.~RHE} = E_{vs.~Ag/AgCl} + 0.197~V + 0.059 \times pH$$

Cyclic voltammogram (CV) was first conducted between 0.00 V to 1.25 V (vs. RHE) with a scanning speed of 500 mV s^{-1} in N$_2$-saturated 0.1 M HClO$_4$. During CO-stripping cyclic voltammograms, constant potential of −15 mV (vs. RHE) was held for 12 minutes in 0.1 M HClO$_4$ electrolyte saturated with CO and then cyclic voltammograms were measured in the potential range of 0–1.25 V with 50 mV s^{-1} in 0.1 M HClO$_4$ electrolyte saturated with N$_2$. Then linear scanning voltammetry (LSV) was conducted to characterize the ORR catalytic activity of samples under following conditions: sweep rate of 10 mV s^{-1}, rotation rate of 1600 rpm and O$_2$-saturated 0.1 M HClO$_4$ solution.

The specific activity (SA) and mass activity (MA) of catalysts were figured out from the polarization curve obtained by LSV. The following Koutecký–Levich equation was applied to calculated the kinetic currents (i_k), representing the intrinsic ORR activity:

$$i_k = \frac{i \times i_d}{i_d - i}$$

where i and i_d were the experimental current and the diffusion limiting current, respectively. For the purpose of measuring the stability of the catalyst, the accelerated durability test (ADT) was implemented by potential sweep cycles in the range of 0.6 to 1.0 V (vs. RHE) for 5000 cycles under the following conditions: scanning speed of 50 mV s^{-1} and O$_2$-saturated 0.1 M HClO$_4$ solution. To obtain a real comparison of the ORR activity of catalyst, iR compensation was taken into consideration. The

resistance was assumed constant during the ORR activity tests and its value was 32 Ω determined by the electrochemical impedance.

3 Results and discussion

3.1 Structure characterizations

Fig. 1 displays the XRD spectra of the Pt$_x$Y/C catalyst prepared by the MSS method. The main diffraction peaks are completely consistent with the reference pattern Pt$_2$Y, in which the obvious peaks at 20°, 39° and 41° are indexed to the (111), (311) and (222) crystal planes of cubic Pt$_2$Y, respectively. In addition, the small broaden peak between 20° and 30° is corresponding to the carbon support. It is worth noting that there are some additional peaks in the XRD spectra, which correspond to those of the Pt$_3$Y reference pattern. The XRD results demonstrate the formation of Pt$_2$Y and Pt$_3$Y alloy phases, among which Pt$_2$Y is the dominant phase.

To further verify the formation of Pt$_x$Y alloys, the high-resolution TEM (HRTEM) and the element mappings of Pt$_x$Y have been provided in Fig. 1b–f. The lattice fringe distance of Pt$_x$Y particles in Fig. 1b is about 0.229 nm, which corresponds to the interplanar distance of (311) crystal plane of Pt$_2$Y. On the other hand, from the element mapping images of Pt$_x$Y displayed in Fig. 1c–f, it is obvious that the Pt and Y elements were distributed in the nanoparticles homogeneously, demonstrating that Pt and Y metals are well alloyed. Besides, Pt$_x$Y nanoalloy particles are well decorated on the carbon support as shown in Fig. 1g, and most of the particles possess a small particle size. Whereas, there are a few particles with larger particle sizes, which may be caused by the aggregation of the particles. According to the particle size statistics in Fig. 1h, the distribution of particle size is in the range of 9 nm to 90 nm, and most of the particle sizes are around 21 nm. In comparison, as shown in Fig. S1,† the average particle size of Pt in JM Pt/C catalyst is around 2 nm. Obviously, the synthesized Pt$_x$Y nanoalloy particles are much larger than the Pt particles of JM Pt/C catalyst due to the high synthesis temperature.

XPS analysis was used to determine the electronic structure changes of Pt. Fig. 2a showed the Pt 4f core level peaks of the Pt$_x$Y/C and JM Pt/C. The zerovalent metallic Pt (Pt^0) peaks of JM
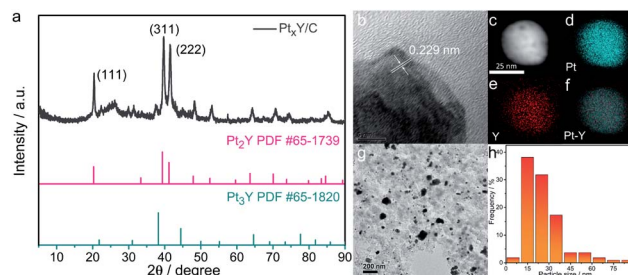

Fig. 1 (a) XRD patterns for the synthesized Pt$_x$Y/C catalysts, (b) HRTEM image of a Pt$_2$Y nanoparticle and (c) HRTEM image of a Pt$_2$Y nanoparticle and its corresponding EDS elemental maps of Pt in blue (e), Y in red (f) and (g) the overlap of Pt and Y, (g) TEM image of Pt$_x$Y/C and its corresponding particle size distribution histogram (h).
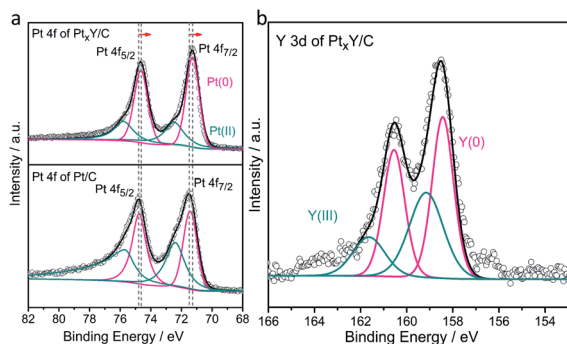
Fig. 2 XPS spectra of (a) Pt 4f core levels for the Pt_xY/C prepared and the JM Pt/C catalysts and (b) Y 3d core levels for the Pt_xY/C prepared.

Pt/C catalyst emerge at 74.8 and 71.4 eV correlating with the Bes of Pt $4f_{5/2}$ and Pt $4f_{7/2}$, respectively. Furthermore, the peaks at about 75.6 (Pt $4f_{5/2}$) and 72.3 eV (Pt $4f_{7/2}$) are on behalf of the Pt^{2+} species. For the Pt_xY/C sample, the Bes of 74.7 and 71.3 eV are assigned to Pt $4f_{5/2}$ and Pt $4f_{7/2}$, separately, corresponding to Pt^0. Meanwhile, the peaks at the Bes of 75.8 eV (Pt $4f_{5/2}$) and 72.5 eV (Pt $4f_{7/2}$) stand for Pt^{2+} species. The Bes of Pt^0 doublet of Pt_xY/C show a negative shift (about 0.1 eV) relative to JM Pt/C catalyst. This negative shift is ascribable to the change in surroundings around the Pt atoms produced by alloying Pt and Y,[39,40] which changes the electronic structure of Pt. Partial hybridization of d–d band takes place when Pt is alloyed with lower electronegativity metals, which causes the charge to be transferred from the lower electronegativity metals (Y) to stronger one (Pt) through the metal bond.[40] The d-band center of surface Pt shifts in the same direction as the surface core level,[39,41,42] so when the Bes of surface Pt shift to the negative direction, the d-band center of Pt downshifts.[39] The Pt 4f shift is a sign of Pt_xY alloy formation,[40] which is in good agreement with the results of XRD and TEM analysis.

The formation of Pt_xY alloys is also confirmed from Y 3d high-resolution XPS spectra, as shown in Fig. 2b. By deconvolving the peaks of Y 3d XPS spectra, the peak at Be. 158.4 eV and 160.5 eV close to Y^0, indicating that the Pt_xY alloys are formed.[43,44] Moreover, the other two peaks at 159.2 and 161.7 eV are represented Y_2O_3.[34] It can be predicted that a small amount of Y_2O_3 will appear on the surface due to the high oxygen affinity of Y. This is different from XRD results, mainly because a small amount of Y_2O_3 on the surface is within the detection limit of XRD measurement, while XPS is surface sensitive.
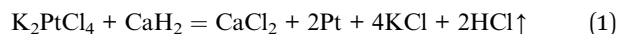
3.2 Synthesis mechanism

According to the differential scanning calorimetr (DSC) and thermogravimetric analysis (TG) curves of K_2PtCl_4 in Fig. 3a, the pure K_2PtCl_4 begins to melt at 370 °C and decomposes accompanied by decalescence and mass loss after heating to 600 °C. As excess CaH_2 is mixed with K_2PtCl_4, the DSC and TG curves in Fig. 3b showed that Pt ions were reduced to metallic Pt at 210 °C in terms of the reaction (1), which also indicates a thermodynamical feasibility based on a negative Gibbs free energy of the reaction. In the temperature range from 210 °C to 600 °C, about

6% of the mass loss of the mixture is observed, which corresponds HCl volatilization and is close to the theoretical value of 8%.

In addition, the TG curve shows an obviously downward trend at 600 °C, which corresponds to the decomposition of excess CaH_2. Therefore, Pt was first formed by the reaction of K_2PtCl_4 and CaH_2 at 210 °C during the synthesis progress of Pt–Y alloy. Afterwards Y ions were preferentially reduced on the Pt surface followed by Pt_xY alloys formation in the molten LiCl–CaH_2 system.

As LiCl is absent in the MSS process of the alloys, only Pt metal is formed without any alloy peaks in the XRD patterns presented in Fig. S2.† This can be predicted according to the phase diagrams of Pt–RE alloys (*e.g.*, Pt–Y, Fig. S3†), which shows that the synthesis temperature of Pt–Y alloy is above 1000 °C. Differently, after adding LiCl, Pt–Y alloy was successfully synthesized (Fig. 1a). This is probably due to the fact that molten LiCl–CaH_2 provides a liquid and strong reaction environment for Pt_xY alloys formation, and lowers the formation temperature of the alloys. The products obtained by MSS after cooled without any treatments were composed of LiCl, $CaCl_2$, CaH_2, CaO and KCl, respectively, as shown in Fig. 3c. The intensity of these products is much higher than that of the Pt–Y alloy, resulting in the alloy phase not being observed. Through the analysis of these byproducts and the previous DSC results, we have summarized the synthesis mechanism and the typical synthesis scheme is described in Scheme 1. In this regard, the possible reactions are proposed as follows:

$$K_2PtCl_4 + CaH_2 = CaCl_2 + 2Pt + 4KCl + 2HCl\uparrow \quad (1)$$

$$\Delta G = -133.583 \text{ kcal mol}^{-1} (200 \text{ °C})$$

$$Y_2O_3 + 2Pt + 3CaH_2 = 2Pt_xY + 3CaO + 3H_2\uparrow \quad (2)$$

Further, Pt_2Gd and Pt_2La alloys were synthesized using the same method, according to the XRD results shown in Fig. 4. The HRTEM and the element mappings in Fig. 5 further verified the formation of Pt_2La and Pt_2Gd alloys. The lattice fringe distances
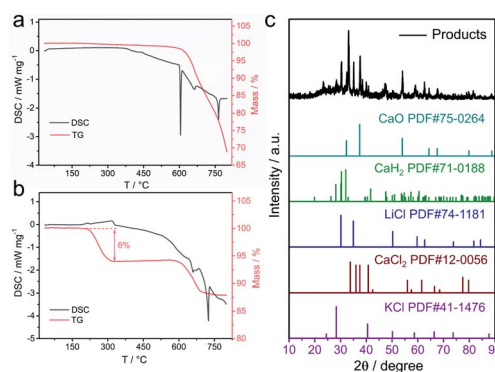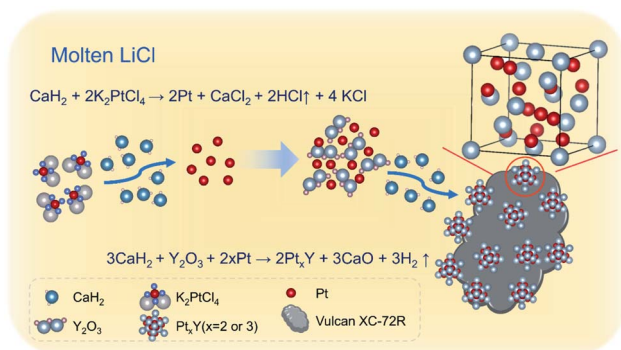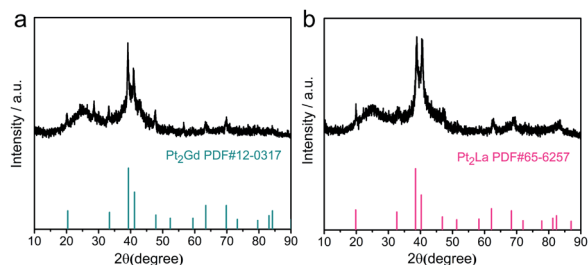

Fig. 3 (a) DSC and TG curves for K_2PtCl_4, (b) DSC and TG curves for a mixture of CaH_2 and K_2PtCl_4, (c) XRD pattern of the materials synthesized without LiCl.

Scheme 1 Process for the synthesis of Pt_xY/C nanoparticles.

Fig. 4 XRD patterns of the synthesized Pt_2Gd/C (a) and Pt_2La/C (b).

(0.449 nm and 0.229) correspond to the interplanar distance of (111) crystal plane of Pt_2La and (311) of Pt_2Gd, respectively. Meanwhile, the element mapping images in Fig. 5b–e and g–j indicates that Pt, La and Gd are uniformly distributed in the

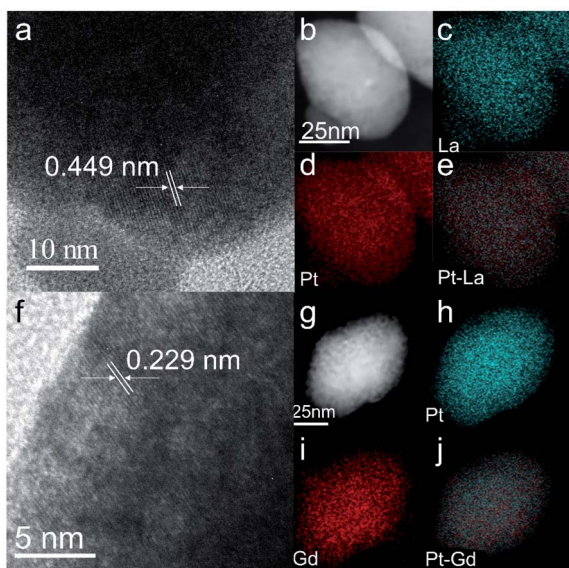**Fig. 5** HRTEM image of a Pt_2La nanoparticle (a) and (b) and its corresponding EDS elemental maps of Pt in red (c), La in blue (d) and (e) the overlap of Pt and La, HRTEM image of a Pt_2Gd nanoparticle (f) and (g) and its corresponding EDS elemental maps of Pt in blue (h), Gd in red (i) and (j) the overlap of Pt and Gd.

particles. The above results prove that Pt_2La and Pt_2Gd alloys have been successfully synthesized.

3.3 Electrochemical properties

Aiming to assess the electrocatalytic properties toward ORR of the catalyst, the ORR polarization curves of these three materials synthesized (Pt_xY/C, Pt_2Gd/C, and Pt_2La/C) and JM Pt/C catalysts were measured in oxygen-saturated 0.1 M $HClO_4$ electrolyte. The results are shown in Fig. 6a, showing that the half-wave potentials of the synthesized materials are all higher than that of JM Pt/C catalyst. Among them, the Pt_xY/C alloy has the highest half-wave potential (0.905 V), which is 25 mV higher than that of the JM Pt/C catalyst (0.88 V), indicating its superior ORR electrocatalytic activity. Furthermore, the half-wave potentials of Pt_2Gd/C and Pt_2La/C are 0.901 V and 0.89 V, which are positively shifted 21 mV and 10 mV compared with the JM Pt/C catalyst, respectively. Fig. 6b shows that the mass activities at 0.9 V (*vs.* RHE) of Pt_xY/C, Pt_2Gd/C and Pt_2La/C are 0.3, 0.25, and 0.17 A mg_{Pt}^{-1}, which are 2.5 times, 2.08 times and 1.42 times as much as JM Pt/C catalysts (0.12 A mg_{Pt}^{-1}), respectively. This corroborates the ORR activity enhancement of Pt–RE metal alloy catalysts. From the CV curves in Fig. 6c, both Pt_xY/C and JM Pt/C show nearly the same trend. On the other hand, as shown by the vertical line in Fig. 6c, the potentials of the oxidation peak and reduction peak of Pt in the Pt_xY/C catalyst shift to higher potentials with respect to JM Pt/C, implying the bonding strength between Pt and oxygenated intermediates is weakened[24,45–47] that is associated with the downshift of d-band center of Pt. Under this circumstance, the weakened bonding could be beneficial to the desorption of oxygenated intermediates on the Pt site, thereby promoting the ORR progress and improving the activity.[48,49] Furthermore, the shift of oxidation peak to a higher potential also illustrates that the adsorption strength between Pt and *O is weakened,[50] which is a sign of enhanced ORR performance.[24] The
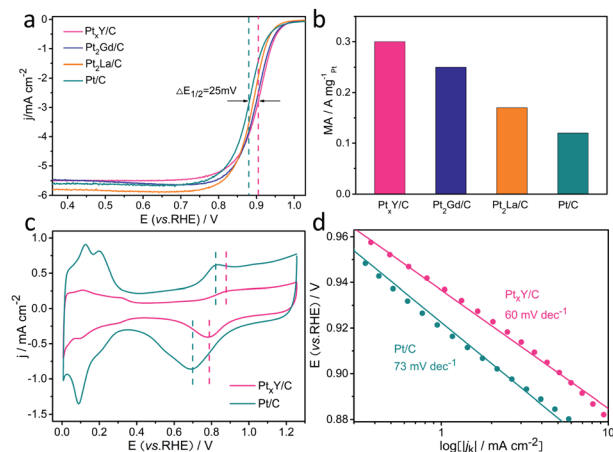

Fig. 6 (a) CVs of Pt_xY/C synthesized and JM Pt/C in 0.1 M $HClO_4$ solution saturated with nitrogen, (b) the ORR LSV curves of Pt_xY/C and JM Pt/C in 0.1 M $HClO_4$ solution saturated with oxygen, (c) Tafel plots for Pt_xY/C synthesized and JM Pt/C, (d) SA and MA of Pt_xY/C synthesized and JM Pt/C.

comparative CO-stripping voltammograms of Pt_xY/C and JM Pt/C catalyst are represented in Fig. S4.† Apparently, the onset potential and the CO stripping peak of Pt_xY/C shifts negatively, illustrating the reduced interaction of Pt–CO and the weaken bonding between Pt and CO.[48] This is also correlated with the downshift of the d-band center of Pt,[48,51] which coincides with the XPS results and the analysis of positive potential shift in Fig. 2a. Additionally, the negative shift of CO stripping peak proves that Pt_xY/C has excellent resistance to CO poisoning on the surface.[52,53]

Fig. 6d presents the Tafel curves of Pt_xY/C and JM Pt/C catalyst. The Tafel slope of Pt_xY/C reveals a smaller value (60 mV dec^{-1}) with respect to that of JM Pt/C catalyst (73 mV dec^{-1}), demonstrating the minor charge transfer resistance and an improvement in ORR kinetics of Pt_xY/C. The improved performance of Pt_xY/C alloys can be put down to the electronic structure changes of Pt influenced by alloying Y with Pt. The d-band center downshift of Pt in Pt_xY/C can decrease the adsorption strength of reaction intermediates (*O, *OH, *OOH) during the ORR, thus enhance the activity of ORR. In brief, we can conclude that the incorporation of RE metal (*e.g.*, Y) and the formation of the alloy between Pt and RE are conducive to enhance the ORR activity through these electrochemical tests.

The durability of the catalysts significantly influences even dominates the practical applications of the catalysts. Therefore, the ADT was performed to assess the durability of the Pt_xY/C and the JM Pt/C catalysts, and the results were shown in Fig. 7a–c. Obviously, the LSV curves of Pt_xY/C and JM Pt/C catalysts both shifted toward to negative potential direction after 5000 potential cycles, indicating the catalytic activity of the catalysts displayed a decreased trend. Pt_xY/C reveals the negative half-wave potential shift of 10 mV with regard to a more obvious shift of 15 mV for the JM Pt/C catalyst, demonstrating the relatively high stability of Pt_xY/C. As shown in Fig. 7c, the initial MA value of Pt_xY/C is 0.26 A mg_{Pt}^{-1}, which is 2.2 times

that of JM Pt/C (0.12 A mg_{Pt}^{-1}). After 5000 cycles, the MAs of Pt_xY/C catalyst (0.19 A mg_{Pt}^{-1}) is about 3 times that of JM Pt/C (0.064 A mg_{Pt}^{-1}). In addition, the Pt_xY/C shows only 27% loss of MA, while the MA of JM Pt/C catalyst decays by 47%. The results reveal that Pt_xY/C has significantly higher durability over JM Pt/C catalyst, which is attributed to the negative alloy formation energy of Pt_xY alloy, therefore leading to a high kinetic stability to prevent continuous dealloying.[43] The nanoparticles of Pt_xY alloys are well-retained after ADT as seen in Fig. S5,† which is conducive to maintaining high performance toward ORR,[54,55] thereby improving its durability. As for the JM Pt/C, the Pt particles have been agglomerated and grown up after durability test in Fig. S6.† Furthermore, the detachment of a few Pt particles from the support leads to the degradation of ORR performance. On the other hand, the XRD spectrum of Pt_xY/C after ADT shown in Fig. S7† indicates that the peaks still correspond to Pt_2Y but the peak shape is not obvious. Compared the Pt 4f XPS spectra before and after ADT in Fig. S8,† the Pt 4f peaks shift to a lower binding energy, indicating an enhanced stress effect, which leads to enhanced adsorption of Pt and O atoms.[55] The above results revealed that after ADT, Pt_xY/C shows a trend of lower catalytic performance.

Chronoamperometry (CA) is measured to study the electrochemical stability of the catalysts, and the results are shown in Fig. 7d–e. The Pt_xY/C and JM Pt/C have shown a sharp drop of the initial currents during the first 400 s, and then a slow drop of currents until 5000 s. Within the initial 100 s, the currents of the Pt_xY/C and JM Pt/C decrease in the same manner. As time goes by, Pt_xY/C has exhibited a slower decrease trend in current than JM Pt/C. It demonstrates that Pt_xY/C has shown better electrochemical stability than JM Pt/C, in good agreement with the ADT assessments. The improvement of durability may be due to the exceptional negative alloy formation energy in the Pt–Y alloy to some extent,[43] which provides a higher kinetic stability
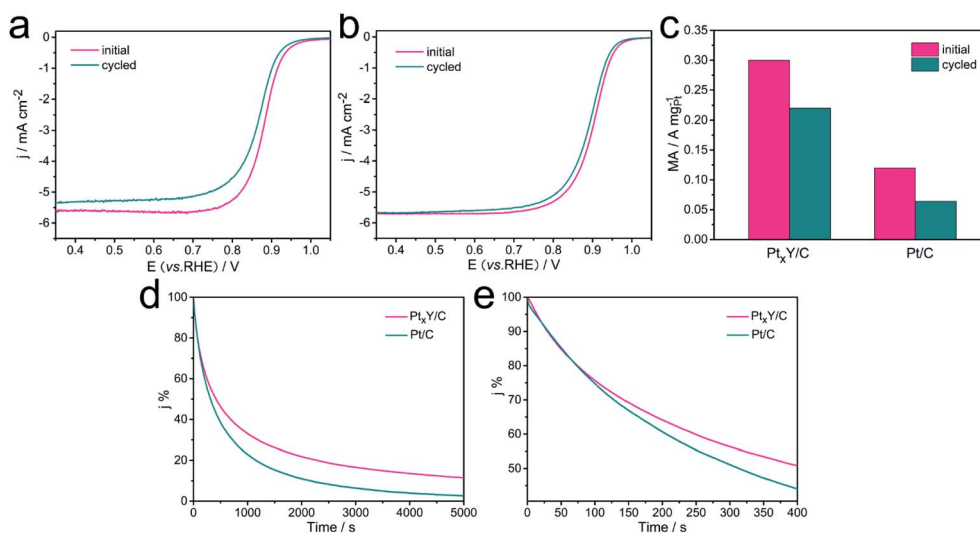

Fig. 7 (a) ORR LSV curves of JM Pt/C before and after 5000 CV cycles, (b) ORR LSV curves of Pt_xY/C synthesized before and after 5000 CV cycles, (c) mass activity of Pt_xY/C synthesized and JM Pt/C before and after 5000 CV cycles, (d) chronoamperometry curves of Pt_xY/C and commercial Pt/C, (e) the first 400 s of chronoamperometry curves of Pt_xY/C and commercial Pt/C.

and can resist continuous dealloying under PEMFC reaction conditions.

The electrochemical performance comparison of this material with Pt₂Y and Pt₃Y alloys recently reported by other researchers is summarized in Table S1.† In this work, the particle size of the obtained material is much larger than that in these literatures, but it still improves the ORR catalytic activity, indicating that the Pt–RE alloys have great potential in catalyzing ORR. The MA and SA are inferior to some previously reported materials, which may be related to the larger particle size of Pt$_x$Y nanoalloy. Indeed, the MA and SA for Pt$_x$Y/C are closely connected with the particle size of Pt$_x$Y and the optimal particle size is approximately 8–9 nm.[44] Most of the synthesized Pt$_x$Y particles have larger particle diameters (>10 nm), which also leads to an insignificant improvement of the half-wave potential. Therefore, it is expected to improve the activity of the material by reducing the particle size.

4 Conclusions

In conclusion, it is the first time that the carbon-supported Pt–RE nanoalloys were successfully synthesized in one step by a simple MSS method, and the synthesis mechanism is discussed in this paper.

Pt$_x$Y/C catalysts with the average particle sizes of around 21 nm, was synthesized by mixing K_2PtCl_4 with Y_2O_3 (in a molar ratio of Pt : Y = 1 : 1) with carbon support in molten LiCl–CaH_2 system by one-step MSS method at 600 °C. Pt₂Gd/C and Pt₂La/C are also obtained with Gd_2O_3 and La_2O_3 as the starting raw materials, respectively by using the same process as above.

In the synthesis processes, Pt nanoparticles were first obtained by the reaction of K_2PtCl_4 and CaH_2 at 210 °C, then Y ions were preferentially reduced on the Pt nanoparticles surface followed by Pt$_x$Y alloys formation in the molten LiCl–CaH_2 system at 600 °C. CaH_2 has the high reduction capacity to extract the oxygen atoms from RE_2O_3, which is beneficial to form Pt–RE alloys. Molten LiCl provides a strong reducing environment and lowers the formation temperature of alloys.

The half-wave potentials of Pt$_x$RE/Cs are all more positive than that of commercial Pt/C catalyst (e.g., 0.905 V for Pt$_x$Y/C while 0.880 V for JM Pt/C). Furthermore, electrochemical characterizations have demonstrated that Pt$_x$Y/C samples show higher electrocatalytic activity toward ORR and preferable catalytic durability with respect to JM Pt/C catalysts. This facile synthesis method provides an effective strategy for the preparation of Pt–RE based multicomponent nanoalloys, especially in a large-scale production.

Conflicts of interest

There are no conflicts to declare.

Acknowledgements

References

1 X. K. Wan, G. Samjeske, H. Matsui, C. Chen, S. Muratsugu and M. Tada, Dalton Trans., 2021, 50, 6811–6822.

2 G. Liu, Z. Yang, X. Wang and B. Fang, Nanomaterials, 2021, 11, 3462.

3 Z. Yang, M. Chen, B. Fang and G. Liu, Nanomaterials, 2020, 10, 2412.

4 T. Zhao, E. Luo, Y. Li, X. Wang, C. Liu, W. Xing and J. Ge, Sci. China Mater., 2021, 64, 1671–1678.

5 Y. J. Wang, D. P. Wilkinson and J. Zhang, Chem. Rev., 2011, 111, 7625–7651.

6 T. Fu, J. Fang, C. Wang and J. Zhao, J. Mater. Chem. A, 2016, 4, 8803–8811.

7 K. M. Naik, E. Higuchi and H. Inoue, J. Power Sources, 2020, 455, 227972.

8 B. Fang, L. Daniel, A. Bonakdarpour, R. Govindarajan, J. Sharman and D. P. Wilkinson, Small, 2021, 17, e2102288.

9 Z. Wang, Z. Lin, J. Deng, S. Shen, F. Meng, J. Zhang, Q. Zhang, W. Zhong and L. Gu, Adv. Energy Mater., 2020, 11, 2003023.

10 C. Huang, W. Dong, C. Dong, X. Wang, B. Jia and F. Huang, Dalton Trans., 2020, 49, 1398–1402.

11 L. Lu, B. Wang, D. Wu, S. Zou and B. Fang, Nanoscale, 2021, 13, 3709–3722.

12 Z. Lin, B. Xiao, Z. Wang, W. Tao, S. Shen, L. Huang, J. Zhang, F. Meng, Q. Zhang, L. Gu and W. Zhong, Adv. Funct. Mater., 2021, 31, 2102321.

13 Z. Wang, Z. Lin, S. Shen, W. Zhong and S. Cao, Chin. J. Catal., 2021, 42, 710–730.

14 B. Fang, B. A. Pinaud and D. P. Wilkinson, Electrocatalysis, 2016, 7, 336–344.

15 Y.-J. Wang, W. Long, L. Wang, R. Yuan, A. Ignaszak, B. Fang and D. P. Wilkinson, Energy Environ. Sci., 2018, 11, 258–275.

16 L. Lu, S. Zou and B. Fang, ACS Catal., 2021, 11, 6020–6058.

17 B. Fang, N. K. Chaudhari, M.-S. Kim, J.-H. Kim and J.-S. Yu, J. Am. Chem. Soc., 2009, 131, 15330–15338.

18 Z. Wang, B. Xiao, Z. Lin, Y. Xu, Y. Lin, F. Meng, Q. Zhang, L. Gu, B. Fang, S. Guo and W. Zhong, Angew. Chem., Int. Ed., 2021, 60, 23388–23393.

19 M.-S. Kim, B. Fang, N. K. Chaudhari, M. Song, T.-S. Bae and J.-S. Yu, Electrochim. Acta, 2010, 55, 4543–4550.

20 S. Ma, J. Deng, Y. Xu, W. Tao, X. Wang, Z. Lin, Q. Zhang, L. Gu and W. Zhong, J. Energy Chem., 2022, 66, 560–565.

21 X. Zou, S. G. Chen, Q. M. Wang, X. Y. Gao, J. Li, J. Li, L. Li, W. Ding and Z. D. Wei, Nanoscale, 2019, 11, 20115–20122.

22 Y. Nie, L. Li and Z. Wei, Chem. Soc. Rev., 2015, 44, 2168–2201.

23 C. Roy, B. P. Knudsen, C. M. Pedersen, A. Velazquez-Palenzuela, L. H. Christensen, C. D. Damsgaard,

I. E. L. Stephens and I. Chorkendorff, *ACS Catal.*, 2018, **8**, 2071–2080.

24 E. B. Tetteh, H. Y. Lee, C. H. Shin, S. H. Kim, H. C. Ham, T. N. Tran, J. H. Jang, S. J. Yoo and J. S. Yu, *ACS Energy Lett.*, 2020, **5**, 1601–1609.

25 S. G. Peera, T. G. Lee and A. K. Sahu, *Sustainable Energy Fuels*, 2019, **3**, 1866–1891.

26 N. Lindahl, E. Zamburlini, L. Feng, H. Grönbeck, M. Escudero-Escribano, I. E. L. Stephens, I. Chorkendorff, C. Langhammer and B. Wickman, *Adv. Mater. Interfaces*, 2017, **4**, 1700311.

27 J. Greeley, I. E. Stephens, A. S. Bondarenko, T. P. Johansson, H. A. Hansen, T. F. Jaramillo, J. Rossmeisl, I. Chorkendorff and J. K. Norskov, *Nat. Chem.*, 2009, **1**, 552–556.

28 S. J. Yoo, S. J. Hwang, J.-G. Lee, S.-C. Lee, T.-H. Lim, Y.-E. Sung, A. Wieckowski and S.-K. Kim, *Energy Environ. Sci.*, 2012, **5**, 7521.

29 Y. Hu, J. O. Jensen, L. N. Cleemann, B. A. Brandes and Q. Li, *J. Am. Chem. Soc.*, 2019, **142**, 953–961.

30 R. Brandiele, A. Guadagnini, L. Girardi, G. Dražić, M. C. Dalconi, G. A. Rizzi, V. Amendola and C. Durante, *Catal. Sci. Technol.*, 2020, **10**, 4503–4508.

31 A. Janghorban, M. Lomello-Tafin, J. M. Moreau and P. Galez, *Intermetallics*, 2010, **18**, 2208–2218.

32 H. Itahara, Y. Takatani, N. Takahashi and S. Kosaka, *Inorg. Chem.*, 2020, **59**(18), 13583–13588.

33 J. N. Schwammlein, G. S. Harzer, P. Pfandner, A. Blankenship, H. A. El-Sayed and H. A. Gasteiger, *J. Electrochem. Soc.*, 2018, **165**, J3173–J3185.

34 J. S. Kanady, P. Leidinger, A. Haas, S. Titlbach, S. Schunk, K. Schierle-Arndt, E. J. Crumlin, C. H. Wu and A. P. Alivisatos, *J. Am. Chem. Soc.*, 2017, **139**, 5672–5675.

35 Y. Kobayashi, S. Tada and R. Kikuchi, *Mater. Adv.*, 2020, **1**, 2202–2205.

36 H. Zhao, C. Yu, H. You, S. Yang, Y. Guo, B. Ding and X. Song, *J. Mater. Chem.*, 2012, **22**, 4780–4789.

37 M. Xiao, B. Luo, M. Konarova, Z. Wang and L. Wang, *Eur. J. Inorg. Chem.*, 2020, **31**, 2942–2949.

38 X. Liu, N. Fechler and M. Antonietti, *Chem. Soc. Rev.*, 2013, **42**, 8237–8265.

39 S. J. Yoo, K. S. Lee, S. J. Hwang, Y. H. Cho, S. K. Kim, J. W. Yun, Y. E. Sung and T. H. Lim, *Int. J. Hydrogen Energy*, 2012, **37**, 9758–9765.

40 R. Brandiele, C. Durante, E. Grądzka, G. A. Rizzi, J. Zheng, D. Badocco, P. Centomo, P. Pastore, G. Granozzi and A. Gennaro, *J. Mater. Chem. A*, 2016, **4**, 12232–12240.

41 M. V. Ganduglia-Pirovano, V. N. a. M. H. Cohen, J. Kudrnovský and I. Turek, *Phys. Rev. B: Condens. Matter Mater. Phys.*, 1996, **54**, 8892–8898.

42 B. Hammer and J. K. Nørskov, *Adv. Catal.*, 2000, **45**, 71–129.

43 R. Cui, L. Mei, G. Han, J. Chen, G. Zhang, Y. Quan, N. Gu, L. Zhang, Y. Fang, B. Qian, X. Jiang and Z. Han, *Sci. Rep.*, 2017, **7**, 41826.

44 P. Hernandez-Fernandez, F. Masini, D. N. McCarthy, C. E. Strebel, D. Friebel, D. Deiana, P. Malacrida, A. Nierhoff, A. Bodin, A. M. Wise, J. H. Nielsen, T. W. Hansen, A. Nilsson, I. E. Stephens and I. Chorkendorff, *Nat. Chem.*, 2014, **6**, 732–738.

45 Y. Wang, D. Sun, M. Wang, Z. Feng and A. S. Hall, *J. Phys. Chem. C*, 2020, **124**, 5220–5224.

46 X. Huang, A. J. Shumski, X. Zhang and C. W. Li, *J. Am. Chem. Soc.*, 2018, **140**, 8918–8923.

47 J. X. Wang, N. M. Markovic and R. R. Adzic, *J. Phys. Chem. B*, 2004, **108**, 4127–4133.

48 Y. Xie, Y. Yang, D. A. Muller, H. D. Abruña, N. Dimitrov and J. Fang, *ACS Catal.*, 2020, **10**, 9967–9976.

49 V. Stamenkovic, B. S. Mun, K. J. Mayrhofer, P. N. Ross, N. M. Markovic, J. Rossmeisl, J. Greeley and J. K. Norskov, *Angew. Chem., Int. Ed. Engl.*, 2006, **45**, 2897–2901.

50 A. L. Strickler, A. Jackson and T. F. Jaramillo, *ACS Energy Lett.*, 2016, **2**, 244–249.

51 T. Bligaard and J. K. Nørskov, *Electrochim. Acta*, 2007, **52**, 5512–5516.

52 D. Y. Wang, H. L. Chou, Y. C. Lin, F. J. Lai, C. H. Chen, J. F. Lee, B. J. Hwang and C. C. Chen, *J. Am. Chem. Soc.*, 2012, **134**, 10011–10020.

53 M. Lokanathan, I. M. Patil, P. Mukherjee, A. Swami and B. Kakade, *ACS Sustainable Chem. Eng.*, 2019, **8**, 986–993.

54 V. T. Ho, C. J. Pan, J. Rick, W. N. Su and B. J. Hwang, *J. Am. Chem. Soc.*, 2011, **133**, 11716–11724.

55 B. Zhang, G. Fu, Y. Li, L. Liang, N. S. Grundish, Y. Tang, J. B. Goodenough and Z. Cui, *Angew. Chem., Int. Ed. Engl.*, 2020, **59**, 7857–7863.